

Far-Infrared Properties of Blue Compact Dwarf Galaxies Observed with AKARI/Far-Infrared Surveyor (FIS)*

Hiroyuki HIRASHITA

Institute of Astronomy and Astrophysics, Academia Sinica, P.O. Box 23-141, Taipei 106, Taiwan
hirashita@asiaa.sinica.edu.tw

Hidehiro KANEDA

Institute of Space and Astronautical Science, Japan Aerospace Exploration Agency, 3-1-1, Yoshinodai, Sagami-hara, Kanagawa
229-8510

Takashi ONAKA

Department of Astronomy, Graduate School of Science, The University of Tokyo, 7-3-1 Hongo, Bunkyo-ku, Tokyo 113-0033
and

Toyoaki SUZUKI

Advanced Technology Center, National Astronomical Observatory of Japan, 2-21-1 Osawa, Mitaka, Tokyo 181-8588

(Received 2008 May 6; accepted 2008 August 7)

Abstract

We report basic far-infrared (FIR) properties of eight blue compact dwarf galaxies (BCDs) observed by AKARI. We measure the fluxes at the four FIS bands (wavelengths of 65 μm , 90 μm , 140 μm , and 160 μm). Based on these fluxes, we estimate basic quantities about dust: dust temperature, dust mass, and total FIR luminosity. We find that the typical dust temperature of the BCD sample is systematically higher than that of normal spiral galaxies, although there is a large variety. The interstellar radiation field estimated from the dust temperature ranges up to 100 times of the Galactic value. This confirms the concentrated star-forming activity in BCDs. The star formation rate can be evaluated from the FIR luminosity as 0.01–0.5 $M_{\odot} \text{ yr}^{-1}$. Combining this quantity with gas mass taken from the literature, we estimate the gas consumption timescales (gas mass divided by the star formation rate), which prove to span a wide range from 1 Gyr to 100 Gyr. A natural interpretation of this large variety can be provided by intermittent star formation activity. We finally show the relation between dust-to-gas ratio and metallicity (we utilize our estimate of dust mass, and take other necessary quantities from the literature). There is a positive correlation between dust-to-gas ratio and metallicity as expected from chemical evolution models.

Key words: galaxies: dwarf — galaxies: ISM — infrared: galaxies — ISM: dust, extinction

1. Introduction

Dust grains absorb stellar ultraviolet (UV)–optical light and reprocess it into far-infrared (FIR), thereby affecting the energetics of interstellar medium. In particular, Hirashita & Ferrara (2002) show that the dust produced by supernovae efficiently absorbs UV heating photons and helps gas cooling and H_2 production even in primeval galaxies (typical age is $< 10^8$ yr). Dust grains also affect the escape fraction of UV photons out of galaxies. Observationally, this means that there is always a correction factor for dust extinction when one estimates star formation rate (SFR) from UV luminosity (Buat & Xu 1996). Indeed, a large correction factor for dust extinction is required for the cosmic star formation rate traced with UV (Steidel et al. 1999; Takeuchi, Buat, & Burgarella 2005; Le Floch et al. 2005; Pérez-González et al. 2005). Also theoretically, how dust accumulates in the history of the Universe is important in the context of the cosmic reionization, because dust absorption affects the escape

fraction of ionizing photons (Ciardi, Bianchi, & Ferrara 2002).

The origin of the cosmic dust is important in itself, and the formation and destruction of grains are tightly related to the star formation activity of galaxies. The condensation of heavy elements is an important process for the formation of grains. In particular, in young galaxies, dust is predominantly condensed in Type II supernovae (SNe II), whose progenitors have short lifetimes (Dwek & Scalo 1980; Kozasa, Hasegawa, & Nomoto 1989; Morgan & Edmunds 2002; Nozawa et al. 2003). However, how much dust forms in a SN II is not known. There is a large difference among observationally derived dust mass (Moseley et al. 1989; Dunne et al. 2003; Hines et al. 2004; Sugerman et al. 2006; Meikle et al. 2007; Ercolano, Barlow, & Sugerman 2007; Rho et al. 2008). Thus, it is important to constrain the dust mass formed in SNe II by quantifying dust mass in young galaxies.

A large amount of dust has been suggested to exist at high redshift (z) (e.g., Bertoldi et al. 2003; Priddey et al. 2003). The estimate of dust mass in high- z galaxies indeed constrains how much dust forms in SNe II (Dwek, Galliano, & Jones 2007). The rest-frame UV extinction

* Based on observations with AKARI, a JAXA project with the participation of ESA.

curves also suggest that dust enrichment by SNe II is indeed occurring at high- z (Maiolino et al. 2004; Bianchi & Schneider 2007; Hirashita et al. 2008). However, it is not easy to explore the first dust enrichment in primeval galaxies at high z ($z \gtrsim 5$) with present observational facilities. Therefore, nearby templates of primeval galaxies are useful to test galaxy formation scenarios. The best candidates for such a template are metal-poor ($\sim 1/10$ – $1/3$ solar) blue compact dwarf galaxies (BCDs), since they are at the early stage of chemical evolution and their typical stellar age is young (Sargent & Searle 1970). Indeed BCDs harbor appreciable quantities of dust (Thuán, Sauvage, Madden 1999; Plante & Sauvage 2002; Hunt et al. 2006), and can be used to investigate the dust properties in chemically unevolved galaxies (Takeuchi et al. 2005).

The dust content in a galaxy is often estimated by measuring the dust emission in FIR. Because of the large all-sky sample, the Infrared Astronomical Satellite (IRAS) 60 μm and 100 μm bands are most frequently used. However, Shibai, Okumura, & Onaka (1999), from the study of FIR spectral energy distribution (SED) of the Milky Way, show that the IRAS bands fail to detect a significant fraction of emission from large grains which contribute to wavelengths (λ) longer than 100 μm (see also Okumura et al. 2002). Moreover, with the size distribution derived for the Milky Way dust grains, the largest contribution to the dust content comes from large grains ($a \sim 0.1 \mu\text{m}$, where a is the grain radius) (Mathis, Rumpl, & Nordsieck 1977). Large grains also have an importance that their temperature reflects the stellar radiation field of interstellar medium through the equilibrium between the heating from stellar radiation and the radiative cooling in FIR (Draine & Anderson 1985). In summary, FIR observation of emission from large grains at $\lambda > 100 \mu\text{m}$ is important to quantify the dust content and the stellar radiation field.

Indeed, Galliano et al. (2005) show that some BCDs have a cold dust component contributing to $\lambda > 100 \mu\text{m}$. Popescu et al. (2002) also point out that BCDs tend to have the coldest dust temperature by using a Virgo cluster sample observed by the Infrared Space Observatory (ISO), although the sample size is small. This is unexpected from the warm IRAS 60 μm /100 μm colors of BCDs (Hoffman et al. 1989). Engelbracht et al. (2008), by using the 70 μm and 160 μm bands of Multiband Imaging Photometer for Spitzer (MIPS) on the Spitzer Space Telescope, show that the dust temperature tends to rise as the metallicity decreases from solar metallicity (Z_{\odot}) to $\sim 1/10 Z_{\odot}$. However, there is a risk of contamination of stochastically heated dust in the 70 μm band (Li & Draine 2001), which leads to overestimation of the large-grain temperature. Thus, a statistical sample at $\lambda > 100 \mu\text{m}$ is indeed required to avoid possible contamination from stochastically heated grains, and simultaneously to overcome the small number statistics of long-wavelength ($\lambda > 100 \mu\text{m}$) observations.

In this paper, we report observations of BCDs in FIR wavelengths including $\lambda > 100 \mu\text{m}$. The data are obtained by AKARI (Murakami et al. 2007) Far-Infrared Surveyor

(FIS) (Kawada et al. 2007). The continuous wavelength coverage ($\lambda \sim 50$ – $180 \mu\text{m}$) and 4 bands in the FIR provided by FIS enable us not only to quantify the long-wavelength ($\lambda > 100 \mu\text{m}$) dust luminosity but also to separate the contribution from stochastically heated grains by using the short-wavelength ($\lambda \lesssim 70 \mu\text{m}$) band. We also demonstrate that this advantage of FIS indeed makes it possible to discuss some quantities related to dust properties and dust enrichment.

This paper is organized as follows. Observations and data reduction are described in section 2. Then, the basic data are shown in section 3, and some quantities derived from those data are presented in section 4. In section 5 we discuss the results, and finally in section 6 we summarize this paper.

2. Observations and Reduction

The observations of eight BCDs are carried out by FIS onboard AKARI as one of the open time observing programs (Proposal ID: BCDDE, PI: H. Hirashita) with four photometric bands of *N60*, *WIDE-S*, *WIDE-L*, and *N160*, whose central wavelengths are 65, 90, 140, and 160 μm with effective band widths of $\Delta\lambda = 21.7, 37.9, 52.4,$ and $35.1 \mu\text{m}$, respectively (Kawada et al. 2007). The measured FWHMs of the point spread function (PSF) are $37 \pm 1''$, $39 \pm 1''$, $58 \pm 3''$, and $61 \pm 4''$, respectively, for the above four bands.

The sample BCDs are listed in Table 1. We primarily selected the sample with IRAS detections as listed in Hirashita, Tajiri, & Kamaya (2002) (originally compiled by Sage et al. 1992 and Lisenfeld & Ferrara 1998). II Zw 40, Mrk 7, UM 439, UM 533, and II Zw 70 are finally observed. The limitation to the sample comes from the lifetime and visibility of the satellite. We also add Mrk 36 and Mrk 71 from Hopkins, Schulte-Ladbeck, & Drozdovsky (2002) since they matched the visibility requirement. Those galaxies are also detected by IRAS. II Zw 71 is also included in the sample, since it lies in the field of view of II Zw 70. This is the only galaxy which is not detected by IRAS. All the sample BCDs are observed with the FIS01 scan sequence (slow-scan observation for photometry), whose total area scanned in the four bands is $15' \times 12'$. Because of the faintness of the sample, we choose the slower scan speed (8 arcsec/sec) and the largest reset interval (2 sec). The observational parameters are also listed in Table 1.

The raw data were reduced by using the FIS Slow Scan Tool (version 20070914).¹ The absolute calibration of the FIS slow-scan data is based on the COBE/DIRBE² measurements of the diffuse sky emission from zodiacal light and interstellar cirrus averaged over areas of several slow-scan observations. Because the detector response is largely affected by a hit of high energy ionizing particle, we use the local flat; that is, we correct the detector sensitivities by assuming uniformity of the sky bright-

¹ <http://www.ir.isas.ac.jp/ASTRO-F/Observation/>.

² <http://cmbdata.gsfc.nasa.gov/product/cobe/>.

Table 1. Observation log.

Name	R.A. (J2000.0)	Dec. (J2000.0)	Date	Observing mode	Scan speed	Reset interval
II Zw 40	5 ^h 55 ^m 42 ^s .6	3°23′31″.8	2006 Sep. 21	FIS01	8″ s ⁻¹	2 s
Mrk 7	7 ^h 28 ^m 11 ^s .4	72°34′23″.4	2006 Oct. 3	FIS01	8″ s ⁻¹	2 s
Mrk 71	7 ^h 28 ^m 42 ^s .8	69°11′21″.4	2006 Oct. 4	FIS01	8″ s ⁻¹	2 s
UM 439	11 ^h 36 ^m 36 ^s .8	0°48′58″.0	2006 Dec. 16	FIS01	8″ s ⁻¹	2 s
UM 533	12 ^h 59 ^m 58 ^s .1	2°02′57″.3	2007 Jan. 4	FIS01	8″ s ⁻¹	2 s
II Zw 70*	14 ^h 50 ^m 56 ^s .5	35°34′17″.6	2007 Jan. 15	FIS01	8″ s ⁻¹	2 s
II Zw 71*	14 ^h 51 ^m 14 ^s .4	35°32′32″.2	2007 Jan. 15	FIS01	8″ s ⁻¹	2 s
Mrk 36	11 ^h 04 ^m 58 ^s .5	29°08′22″.1	2007 May 27	FIS01	8″ s ⁻¹	2 s

* II Zw 70 and II Zw 71 lie in the same field of view.

ness (Verdugo, Yamamura, & Pearson 2007).³ By using some relatively bright sources, we confirmed that the errors caused by the smoothing procedures are well within 10% for *N60* (65 μm) and *WIDE-S* (90 μm) and 20% for *WIDE-L* (140 μm). These error levels are consistent to or somewhat larger than the background fluctuation mainly caused by a hit of high energy ionizing particle, which implies that the background fluctuation is a major component in the errors. The above values are adopted for the errors in Table 1 except for the following two cases: (i) For the *N60* (65 μm) flux of Mrk 7, we adopt the root-mean-square (rms) of the background fluctuation. (ii) The uncertainty in the *WIDE-S* (90 μm) data of II Zw 70 is also large because of a bad pixel within the aperture radius (section 3.3). For *N160* (160 μm), because of high fluctuation of the background, we adopt the 25% error after estimating the uncertainty in the background subtraction. When the flux is smaller than the rms of the background, we adopt 3 times the background uncertainty as an upper limit.

Our sample BCDs are compact enough to be treated as point sources with the resolution of FIS (but see section 3.3 for Mrk 71). We follow the aperture photometry described in Verdugo, Yamamura, & Pearson (2007). We adopt aperture radii of 0.625 arcmin for *N60* (60 μm) and *WIDE-S* (90 μm) and of 0.750 arcmin for *WIDE-L* (140 μm) and *N160* (160 μm), and sky regions between 2.25 and 3.25 arcmin for *N60* (65 μm) and *WIDE-S* (90 μm) and between 3.0 and 4.0 arcmin for *WIDE-L* (140 μm) and *N160* (160 μm). Then the aperture correction factors (1.58, 1.74, 1.71, and 2.03 for *N60*, *WIDE-S*, *WIDE-L*, and *N160*, respectively) are multiplied to obtain the total flux.⁴

³ We referred to AKARI FIS Data User Manual Version 2 available at <http://www.ir.isas.ac.jp/ASTRO-F/Observation/>. When we run the pipeline command `ss_run_ss`, we apply options `/local,/smooth,width_filter=80`: The flat field is built from the observed sky, and boxcar smoothing with a filter width of 80 s in the time series data is applied to remove remaining background offsets among the pixels.

⁴ We also multiplied another factor called correction factor. It is an empirical factor to correct the discrepancy between the calibration of the diffuse emission (on which the present reduction is based) and that for point sources. This correction factor is empirically known to be constant. By using a different tool developed by T. Suzuki, who adopt point source calibrations by

Finally, color corrections are applied for the *WIDE-L* (140 μm) fluxes: the color correction factor is assumed to be 0.93 (the flux is divided by this factors), which is valid for the temperature range derived by using 140 μm and 90 μm fluxes (22–53 K for $\beta=1$ and 19–36 K for $\beta=2$; see section 4.1) within 3%. For the *WIDE-S* (90 μm) band, color correction would be required. The correction factor is 0.94 at 35 K and 1.06 at 50 K for $\beta=1$, and 0.94 at 30 K and 1.06 at 40 K. These temperature ranges cover the average of 140 μm –90 μm temperature and 65 μm –90 μm temperature (section 4.1). For II Zw 71, whose temperature is significantly lower than the above ranges, upward $\sim 10\%$ correction would be required. However, we do not apply color correction to the *WIDE-S* (90 μm) flux, because the emission in this band may not be described with a single-temperature emission and because the correction factor is not uniform within the sample (i.e., an iteration between the derived dust temperature and color correction is required for each object). For *N60* (65 μm) and *N160* (160 μm), we do not apply color correction, since the color correction change the flux only $< 4\%$ for our sample within the range of dust temperature derived for our sample in section 4.1.

3. Results

3.1. Flux

In Table 2, we present the measured fluxes. All the BCDs are detected in *N60* (65 μm), *WIDE-S* (90 μm), and *WIDE-L* (140 μm) bands except for Mrk 36 (section 3.3). For the *N160* (160 μm) band, a half of the objects are detected and only upper limits are determined for the other half. For comparison, in Table 2 we also compile the IRAS 60 μm and 100 μm fluxes if available. We adopt those data from Moshir et al. (1990) except for II Zw 40, Mrk 71 and II Zw 71 (section 3.3). For II Zw 40, we also present the data taken by Spitzer MIPS at $\lambda=70$ μm and 160 μm (Engelbracht et al. 2008).

asteroids, we confirmed that the correction factors are reasonable within the errors put in this paper. See also Kawada et al. (2007) for the absolute calibration.

Table 2. Measured fluxes.

Name	<i>N60</i> ($\lambda = 65 \mu\text{m}$)	<i>WIDE-S</i> ($\lambda = 90 \mu\text{m}$)	<i>WIDE-L</i> ($\lambda = 140 \mu\text{m}$)	<i>N160</i> ($\lambda = 160 \mu\text{m}$)	IRAS ($\lambda = 60 \mu\text{m}$)	IRAS ($\lambda = 100 \mu\text{m}$)
II Zw 40*	$6.9 \pm 0.7 \text{ Jy}$	$6.6 \pm 0.7 \text{ Jy}$	$3.7 \pm 0.7 \text{ Jy}$	$3.4 \pm 0.9 \text{ Jy}$	$6.61 \pm 0.7 \text{ Jy}$	$5.8 \pm 0.9 \text{ Jy}$
Mrk 7	$0.83 \pm 0.23 \text{ Jy}$	$0.84 \pm 0.08 \text{ Jy}$	$1.1 \pm 0.2 \text{ Jy}$	$1.0 \pm 0.3 \text{ Jy}$	$0.48 \pm 0.04 \text{ Jy}$	$0.97 \pm 0.14 \text{ Jy}$
Mrk 71 [†]	$3.7 \pm 0.4 \text{ Jy}$	$3.1 \pm 0.3 \text{ Jy}$	$2.2 \pm 0.4 \text{ Jy}$	$< 3.0 \text{ Jy}$	$4.83 \pm 0.04 \text{ Jy}$	$5.71 \pm 0.03 \text{ Jy}$
UM 439	$0.42 \pm 0.04 \text{ Jy}$	$0.40 \pm 0.04 \text{ Jy}$	$0.31 \pm 0.06 \text{ Jy}$	$< 0.45 \text{ Jy}$	$0.36 \pm 0.05 \text{ Jy}$	$0.81 \pm 0.11 \text{ Jy}$
UM 533	$0.54 \pm 0.05 \text{ Jy}$	$0.61 \pm 0.06 \text{ Jy}$	$0.54 \pm 0.11 \text{ Jy}$	$< 0.68 \text{ Jy}$	$0.50 \pm 0.05 \text{ Jy}$	$0.54 \pm 0.13 \text{ Jy}$
II Zw 70	$0.89 \pm 0.09 \text{ Jy}$	$0.80 \pm 0.24 \text{ Jy}$	$0.75 \pm 0.15 \text{ Jy}$	$0.62 \pm 0.16 \text{ Jy}$	$0.71 \pm 0.05 \text{ Jy}$	$1.24 \pm 0.12 \text{ Jy}$
II Zw 71	$0.32 \pm 0.03 \text{ Jy}$	$0.54 \pm 0.05 \text{ Jy}$	$1.3 \pm 0.26 \text{ Jy}$	$1.3 \pm 0.3 \text{ Jy}$	—	—
Mrk 36	$0.33 \pm 0.03 \text{ Jy}$	$0.26 \pm 0.03 \text{ Jy}$	$< 0.30 \text{ Jy}$	$< 0.38 \text{ Jy}$	$0.23 \pm 0.06 \text{ Jy}$	$0.68 \pm 0.08 \text{ Jy}$

Note. 3σ upper limits are shown by “<” (For the *WIDE-L* data of Mrk 36, see section 3.3). “—” indicates no data. IRAS $60 \mu\text{m}$ and $100 \mu\text{m}$ data are also shown for comparison in the last two columns.

* II Zw 40 has also Spitzer MIPS data ($5.58 \pm 0.28 \text{ Jy}$ at $\lambda = 70 \mu\text{m}$ and $3.14 \pm 0.43 \text{ Jy}$ at $\lambda = 160 \mu\text{m}$; Engelbracht et al. 2008).

[†] The discrepancy between our results and the IRAS data may be explained by different resolution (section 3.3).

3.2. FIR Spectral Energy Distributions

The data in Table 2 are displayed in Figure 1. For almost all the sources with available IRAS data, the AKARI and IRAS fluxes are consistent but there is a significant discrepancy between the IRAS $100 \mu\text{m}$ flux ($1.24 \pm 0.12 \text{ Jy}$) and the AKARI $90 \mu\text{m}$ ($0.80 \pm 0.24 \text{ Jy}$) flux for II Zw 70. Note that the error bar for the $90 \mu\text{m}$ flux is large because of the bad pixel (section 2). However, we should note that the discrepancy seems significant even after considering the uncertainty in the interpolation. Another possible reason is that the IRAS flux is sometimes overestimated (Jeong et al. 2007). Source confusion could explain the discrepancy, but there is no evidence for a large sky fluctuation around II Zw 70 in our image.

The *N160* ($160 \mu\text{m}$) flux, when detected, is always near to the *WIDE-L* ($140 \mu\text{m}$). Thus, the $160 \mu\text{m}$ flux does not provide strongly independent information of the $140 \mu\text{m}$ flux. Because of this and of a large fraction of non-detection, we do not use $160 \mu\text{m}$ data in the following discussions. Nevertheless, it is worth stressing that the consistency between the $140 \mu\text{m}$ and $160 \mu\text{m}$ fluxes confirms the reliability of the *N160* band. The *N160* flux of II Zw 40 is also consistent with the Spitzer $160 \mu\text{m}$ flux, which also strengthens the reliability of the *N160* fluxes.

3.3. Remarks on individual objects

II Zw 40 — The IRAS data are taken from Vader et al. (1993) (see also Beck et al. 2002). The Spitzer MIPS data are also available in Engelbracht et al. (2008).

Galliano et al. (2005) investigate this galaxy by using detailed SED models. They suggest a very cold dust contributing to the emission at $\lambda \gtrsim 300 \mu\text{m}$ (see also sections 4.5 and 5.2). However, we cannot constrain the dust emission at such a long wavelength range. Hunt, Bianchi, & Maiolino (2005) also study the SED over a wide wavelength range including FIR, and state that the FIR SED has a peak at $\lambda \lesssim 60 \mu\text{m}$, which is consistent with our data. This galaxy has the strongest interstellar radiation field, which supports high density of star formation (Beck et al. 2002; Vanzi et al. 2008).

Mrk 71 — This is called “cometary” BCD (Noeske et al. 2000) and given an NGC number NGC 2366. This is the nearest BCD of our sample with distance of 3.4 Mpc (Tolstoy et al. 1995). Indeed, an extended structure in the north-east direction from the main H II complex NGC 2363 is seen in optical images. Since this paper treats the main star-forming region of a BCD, we concentrate on the main complex, which can be treated as a point source with the resolution of FIS. The north-east extension is detected in the *N60* ($65 \mu\text{m}$), *WIDE-S* ($90 \mu\text{m}$), and *WIDE-L* ($140 \mu\text{m}$) band images. This extended structure does not affect our analysis because of its low surface brightness within the aperture used for the photometry.

With IRAS data, Mazzarella, Bothun, & Boroson (1991) derived larger FIR fluxes (4.829 Jy at $\lambda = 60 \mu\text{m}$ and 5.713 Jy at $\lambda = 100 \mu\text{m}$) than our estimate. In the north-west extension, there is a brightness peak at distance of $\sim 3'$ from the main body. The flux around this peak is preliminarily estimated as 0.7 Jy at $\lambda = 90 \mu\text{m}$ and 0.5 Jy at $\lambda = 65 \mu\text{m}$. This peak can be contaminated with the main body with the resolution of IRAS ($\sim 2' - 5'$) (Neugebauer et al. 1984). Thus, we do not compare AKARI and IRAS results for this galaxy (section 3.2). A quantitative and detailed analysis of the north-east extension will be reported in a separate paper.

II Zw 70 — There is a bad pixel within the photometric radius in *WIDE-S*. Although the brightness of the pixel is extrapolated by using the value of the surrounding pixels, the uncertainty caused by this extrapolation may be as large as 30%.⁵ Thus, we put a 30% error bar to the *WIDE-S* ($90 \mu\text{m}$) flux.

II Zw 71 — This galaxy is occasionally detected in the same field of II Zw 70. It is located at the edge of the field of view, but the aperture used to determine the flux is well within the field. Although the area for the background is smaller than the other sources, the number of background pixels is large enough to subtract the background within

⁵ We derived this error by using another analysis tool developed by Suzuki et al. (2008).

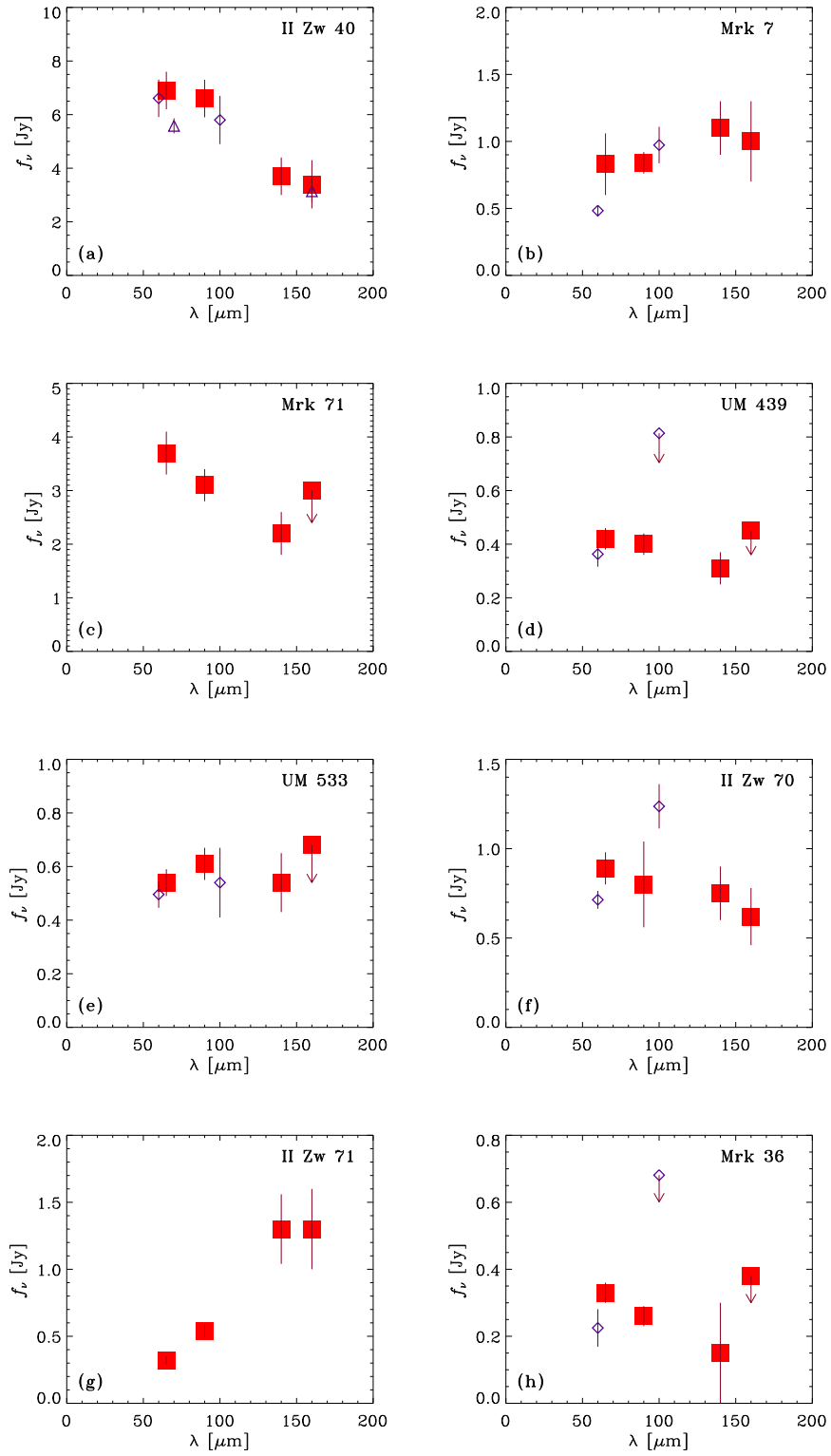


Fig. 1. Observed FIR SEDs at various bands (f_ν is flux in units of Jy and λ is wavelength in units of μm). AKARI data are shown by filled squares and IRAS data are also presented by open diamonds for comparison. For II Zw 40, Spitzer data are available and are shown by open triangles. The bars indicate errors and the points with arrows give 3σ upper limits. The name of object is shown in each panel.

errors of 10% for *N60* (65 μm) and *WIDE-S* (90 μm), 20% for *WIDE-L* (140 μm), and 25% for *N160* (160 μm). This galaxy is not detected by IRAS.

Mrk 36 — This is the faintest object in *WIDE-S*. This galaxy is detected by IRAS at $\lambda = 60 \mu\text{m}$ with a flux level of $0.022 \pm 0.05 \text{ Jy}$ and is not detected at $\lambda = 100 \mu\text{m}$ with an upper limit of 0.68 Jy (Moshir et al. 1990). In the *WIDE-L* image, it seems that relatively bright pixels are clustered in the expected position of Mrk 36. If we use those clustered bright pixels and subtract the background, the flux is 0.15 Jy. But since the uncertainty in the background is comparable to this value, it is safe to put an upper limit of 0.30 Jy.

4. Derived Quantities

4.1. Dust temperature

One of the most straightforward quantities derived by our observations is colors (i.e., flux ratios between two bands), which reflect dust temperatures. In Table 3, we show the colors. Since the *WIDE-S* (90 μm) band is the most sensitive, we present the color relative to 90 μm flux. We denote the flux ratio between wavelengths λ_1 [μm] and λ_2 [μm] as $[\lambda_1, \lambda_2]$. The error of a flux ratio f_1/f_2 , where we denote the errors of f_1 and f_2 as $\text{err}(f_1)$ and $\text{err}(f_2)$, respectively, is estimated by using a simple discussion of error propagation as

$$\text{err}\left(\frac{f_1}{f_2}\right) = \frac{f_1}{f_2} \sqrt{\frac{\text{err}(f_1)^2}{f_1^2} + \frac{\text{err}(f_2)^2}{f_2^2}}. \quad (1)$$

We compare the derived colors with other available samples of star-forming galaxies observed by AKARI FIS. To date, FIS observations of three spiral galaxies have been published to date (Kaneda et al. 2007; Suzuki et al. 2007) as shown in Table 3. We observe that the derived colors of the BCDs show higher temperatures (i.e., larger [65, 90] and smaller [140, 90]) than the spiral galaxies except for Mrk 7 and II Zw 71. This supports the idea that BCDs host intense star formation activities in concentrated regions.

We have selected the present sample primarily from the IRAS catalog. Since intense star formation tends to raise FIR luminosity, our sample may be biased to objects with intense star formation. Indeed, II Zw 71, which is not detected by IRAS, has the lowest dust temperature, and this fact implies a possibility that our selection by IRAS detection is biased to high dust temperature.

Now we estimate the dust temperature from the flux ratio. We fit $A\nu^\beta B_\nu(T_d)$ (A is a constant, $B_\nu(T)$ is the Planck function evaluated at frequency ν and temperature T and β is the index of the emission coefficient called emissivity index) to the fluxes at two bands to derive the dust temperature T_d . Note that A can be eliminated if we take a flux ratio. In Table 3, we show the estimated dust temperature, where $T_d(C; \beta)$ represents the dust temperature derived from color C and emissivity index β .

From Table 3, we observe that the values of T_d is higher for $\beta = 1$ than for $\beta = 2$, because under fixed fluxes at two

wavelengths $\beta = 2$ requires lower T_d (i.e., enhanced $B_\nu(T_d)$ at the longer wavelength) to compensate for lower emission coefficient at the longer wavelength. Again we confirm that the dust temperature of the BCDs is significantly higher than that of the spiral sample except for Mrk 7 and II Zw 71. We also see that there is a large variety of dust temperatures among our sample. Such a large variety of dust temperatures is also reported by Engelbracht et al. (2008) for a low-metallicity sample. One of their sample, II Zw 40 is common with Engelbracht et al. (2008), and the dust temperature derived by them by using the Spitzer 70 and 160 μm bands with $\beta = 2$ is $33.4 \pm 1.0 \text{ K}$, consistent with our $T_d([140/90]; \beta = 2) = 36^{+8}_{-4} \text{ K}$.

If $T_d([65/90])$ is equal to $T_d([140/90])$,⁶ the fluxes in the three bands can be fitted with a single dust temperature. The difference between $T_d([65/90])$ and $T_d([140/90])$ is significant for Mrk 7 and II Zw 71 if $\beta = 1$, and for Mrk 7, Mrk 71, UM 439, UM 533, and II Zw 71 if $\beta = 2$. In those BCDs, $T_d([65/90])$ is higher than $T_d([140/90])$, which possibly indicates that the contribution from stochastically heated grains to the 65 μm flux is prominent compared with the short-wavelength tail of the emission at $\lambda > 90 \mu\text{m}$ (Draine & Li 2001). Since the emission at $\lambda > 90 \mu\text{m}$ comes from dust grains in temperature equilibrium between the heating from stellar radiation field (called interstellar radiation field) and the cooling by FIR reemission, observations by the *WIDE-S* and *WIDE-L* bands are essential to estimate the equilibrium grain temperature. In such a case, the dust temperature derived from the IRAS 60 μm and 100 μm bands is overestimate for the equilibrium grain temperature. For BCDs in which $T_d([65/90])$ is consistent with $T_d([140/90])$, on the contrary, the IRAS 60 μm and 100 μm bands have given reasonable estimate for the equilibrium dust temperature. In this case, the Spitzer 70 μm and 160 μm bands also provide the equilibrium grain temperature.

It is worth noting that as demonstrated above the AKARI FIS bands have the following two advantages: One is that two bands, *WIDE-S* (90 μm) and *WIDE-L* (140 μm), are available to estimate the equilibrium grain temperature, while the Spitzer 70 μm and 160 μm bands have risk of overestimating the equilibrium grain temperature because of the contribution from stochastically heated grains to $\lambda = 70 \mu\text{m}$. (But a wide band has a disadvantage in determining the flux density. In fact the color correction factor is relatively large for *WIDE-S* (90 μm) and *WIDE-L* (140 μm) as stated in section 2.) The other is that the *N60* band (65 μm) is also crucial to estimate the contribution from stochastically heated grains. Thus, the three bands of FIS adopted in this paper provide a unique opportunity to investigate *both* equilibrium-temperature dust and stochastically heated dust.

⁶ When the parameter β is omitted, the statement is true for any β .

Table 3. Flux ratios and dust temperatures.

Name	[65/90]	[140/90]	$T_d([65/90]; 1)$	$T_d([140/90]; 1)$	$T_d([65/90]; 2)$	$T_d([140/90]; 2)$
II Zw 40	1.0 ± 0.15	0.56 ± 0.12	50^{+7}_{-6} K	53^{+20}_{-9} K	39^{+4}_{-3} K	36^{+8}_{-4} K
Mrk 7	0.99 ± 0.29	1.3 ± 0.3	48^{+13}_{-11} K	28^{+4}_{-2} K	38^{+7}_{-7} K	23^{+3}_{-1} K
Mrk 71	1.2 ± 0.2	0.71 ± 0.15	57^{+9}_{-8} K	42^{+10}_{-5} K	43^{+5}_{-4} K	31^{+5}_{-3} K
UM 439	1.1 ± 0.15	0.78 ± 0.17	50^{+7}_{-5} K	39^{+10}_{-5} K	39^{+4}_{-3} K	30^{+4}_{-3} K
UM 533	0.89 ± 0.12	0.89 ± 0.20	44^{+5}_{-4} K	36^{+7}_{-5} K	35^{+3}_{-2} K	28^{+4}_{-3} K
II Zw 70	1.1 ± 0.35	0.94 ± 0.34	53^{+19}_{-14} K	34^{+15}_{-5} K	41^{+10}_{-9} K	27^{+8}_{-4} K
II Zw 71	0.59 ± 0.08	2.4 ± 0.5	34^{+2}_{-2} K	22^{+2}_{-2} K	29^{+1}_{-2} K	19^{+1}_{-2} K
Mrk 36	1.3 ± 0.2	0.58 ± 0.58	61^{+11}_{-9} K	> 30 K	45^{+6}_{-5} K	> 24 K
NGC 2841	0.29 ± 0.08	1.9 ± 0.7	24^{+2}_{-3} K	24^{+6}_{-3} K	21^{+2}_{-2} K	20^{+4}_{-2} K
NGC 2976	0.43 ± 0.12	1.14 ± 0.41	29^{+3}_{-4} K	31^{+10}_{-5} K	25^{+3}_{-3} K	25^{+6}_{-3} K
M 101	0.36 ± 0.10	2.1 ± 0.8	27^{+3}_{-4} K	23^{+5}_{-3} K	23^{+3}_{-2} K	19^{+4}_{-1} K

Note. Lower limits are shown by “>”. The last three galaxies are spiral galaxies for comparison. The data are taken from Kaneda et al. (2007) for NGC 2841 and NGC 2976 and from Suzuki et al. (2007) for M 101.

4.2. Interstellar radiation field

Since the dust temperature is determined by the equilibrium between the heating from interstellar radiation field and the cooling by FIR reemission, it is possible to estimate the interstellar radiation field from the equilibrium dust temperature. We adopt $T_d([140/90])$ as the equilibrium grain temperature. The 140 μm –100 μm color of the Galactic disk is concentrated around 2.0 (Hibi et al. 2006; Hirashita, Hibi, & Shibai 2007), which corresponds to the dust temperature of 20.2 K for $\beta = 1$ and 17.3 K for $\beta = 2$. Assuming that the dust heating is dominated by UV radiation (Buat & Xu 1996), we estimate the UV radiation field from the dust temperature. The UV radiation field normalized to the Galactic value is denoted as G_{UV} . Using the scaling relation of $G_{\text{UV}} \propto T_d^{4+\beta}$ (Evans 1995), we obtain

$$G_{\text{UV}}(\beta) = \begin{cases} \left(\frac{T_d}{20.2 \text{ K}} \right)^5 & \text{if } \beta = 1, \\ \left(\frac{T_d}{17.3 \text{ K}} \right)^6 & \text{if } \beta = 2. \end{cases} \quad (2)$$

In Table 4, we present $G_{\text{UV}}(\beta)$ for $\beta = 1$ and 2. Naturally we confirm the above conclusion that the UV interstellar radiation field in BCDs is systematically higher than that in spiral galaxies, although Mrk 7 and II Zw 71 are exceptions. Moreover, there is little difference in G_{UV} between $\beta = 1$ and 2. Thus, it is more useful to adopt G_{UV} instead of T_d to avoid the dependence on β .

4.3. Total FIR luminosity

Total FIR luminosity reflects how much stellar light is absorbed and reemitted by dust grains. It is empirically known that FIR luminosity is a good indicator of SFR in galaxies (Kennicutt 1998; Inoue, Hirashita, & Kamaya 2000). Here we estimate the total FIR luminosity of each BCD. The FIS *N60* (65 μm), *WIDE-S* (140 μm), and *WIDE-L* (140 μm) bands have the advantage of covering *continuously* the wavelength range from 50 μm to 170 μm (Kawada et al. 2007). Thus, by using those three bands,

we define the *AKARI FIR flux*, f_{AKARI} , as an estimate of the flux in the above wavelength range:

$$f_{\text{AKARI}} \equiv f_\nu(65 \mu\text{m})\Delta\nu(N60) + f_\nu(90 \mu\text{m})\Delta\nu(WIDE-S) + f_\nu(140 \mu\text{m})\Delta\nu(WIDE-L), \quad (3)$$

where $f_\nu(\lambda)$ is the flux per unit frequency at wavelength λ , and $\Delta\nu(\text{band})$ denotes the frequency width covered by the band. According to Kawada et al. (2007), we adopt $\Delta\nu(N60) = 1.58$ THz, $\Delta\nu(WIDE-S) = 1.47$ THz, and $\Delta\nu(WIDE-L) = 0.831$ THz. With f_{AKARI} , we define the *AKARI FIR luminosity*, L_{AKARI} , as an estimate of the luminosity in $\lambda = 50$ –170 μm :

$$L_{\text{AKARI}} \equiv 4\pi D^2 f_{\text{AKARI}}, \quad (4)$$

where D is the distance to the object. In Table 4, we list the estimated AKARI FIR luminosities as well as the distances. The distances are taken from Tolstoy et al. (1995) for Mrk 71 (NGC 2366), Osman, Ella, & Issa (1982) for NGC 2841, Karachentsev et al. (2002) for NGC 2976, and Jurcevic & Butcher (2006) for M 101. For more distant galaxies, we estimate the distance from the Galactocentric velocity (taken from NED)⁷ by assuming a Hubble constant of 75 $\text{km s}^{-1} \text{Mpc}^{-1}$.

It is also possible to estimate the FIR luminosity including $\lambda > 170 \mu\text{m}$ by assuming a functional form of $\propto \nu^\beta B_\nu(T_d)$, where we adopt $T_d = T_d([140/90])$. Then we obtain an estimate of the total FIR luminosity at $\lambda > 50 \mu\text{m}$. Following the procedure in Nagata et al. (2002), we estimate the total FIR luminosity as below.

First, we estimate the total FIR flux. The total FIR flux, f_{FIR} , can be well approximated by (Nagata et al. 2002)

$$f_{\text{FIR}} \simeq \int_0^\infty \Omega\tau_{90} \left(\frac{\nu}{\nu_{90}} \right)^\beta B_\nu(T_d) d\nu + \left[f_\nu(65 \mu\text{m}) - B_\nu(65 \mu\text{m}, T_d) \right]$$

⁷ <http://nedwww.ipac.caltech.edu/>.

Table 4. Summary of the properties.

Name	D [Mpc]	G_{UV}		L_{AKARI} [L_{\odot}]	L_{FIR}		M_d	
		$(\beta = 1)$	$(\beta = 2)$		$(\beta = 1)$ [L_{\odot}]	$(\beta = 2)$ [L_{\odot}]	$(\beta = 1)$ [M_{\odot}]	$(\beta = 2)$ [M_{\odot}]
II Zw 40	9.2	120^{+400}_{-70}	81^{+170}_{-42}	6.2×10^8	1.1×10^9	8.1×10^8	3.9×10^4	1.1×10^5
Mrk 7	42.4	$5.4^{+4.9}_{-2.0}$	$5.7^{+4.8}_{-2.0}$	1.9×10^9	2.3×10^9	2.2×10^9	1.4×10^6	3.7×10^6
Mrk 71	3.4	39^{+77}_{-20}	34^{+46}_{-16}	4.4×10^7	5.7×10^7	5.0×10^7	5.4×10^3	1.5×10^4
UM 439	13.1	28^{+52}_{-14}	25^{+35}_{-11}	8.1×10^7	1.0×10^8	9.1×10^7	1.4×10^4	3.7×10^4
UM 533	10.9	17^{+29}_{-8}	16^{+23}_{-7}	8.1×10^7	9.9×10^7	9.1×10^7	2.2×10^4	5.8×10^4
II Zw 70	17.0	14^{+70}_{-8}	14^{+49}_{-8}	2.9×10^8	3.4×10^8	3.2×10^8	8.1×10^4	2.1×10^5
II Zw 71	18.5	$1.4^{+0.9}_{-0.4}$	$1.5^{+1.0}_{-0.5}$	2.5×10^8	3.9×10^8	3.5×10^8	1.0×10^6	2.5×10^6
Mrk 36	8.2	> 7.6	> 7.9	2.2×10^7	—*	—*	$> 8.2 \times 10^2$	$> 1.5 \times 10^3$
NGC 2841	8.1	$2.3^{+4.6}_{-1.1}$	$2.5^{+4.6}_{-1.2}$	1.5×10^9	2.1×10^9	1.9×10^9	3.7×10^6	9.3×10^6
NGC 2976	3.6	$7.8^{+27}_{-4.3}$	$8.1^{+23}_{-4.3}$	4.7×10^8	5.8×10^8	5.5×10^8	3.1×10^5	8.1×10^5
M 101	7.4	$1.8^{+3.3}_{-0.8}$	$2.0^{+3.4}_{-0.9}$	1.1×10^{10}	1.6×10^{10}	1.5×10^{10}	3.4×10^7	8.5×10^7

Note. The last three galaxies are spiral galaxies for comparison (same as Table 3). Lower limits are shown by “>”.

* For Mrk 36, it is not possible to estimate L_{FIR} because $T_d[140/90]$ is not determined.

$$\times \Omega \tau_{90} \left(\frac{65}{90} \right)^{-\beta} \Big] \Delta \nu(N60), \quad (5)$$

where Ω is the solid angle of the object, τ_{90} is the optical depth at $\lambda = 90 \mu\text{m}$, ν_{90} is the frequency corresponding to $\lambda = 90 \mu\text{m}$ (i.e., 3.33 THz), and $B_{\nu}(\lambda, T_d)$ is the Planck function evaluated at wavelength λ . The first term represents the total FIR flux from grains in radiative equilibrium, and the second term shows the contribution of the excess emission of stochastically heated grains in $N60$ ($65 \mu\text{m}$). Thus, f_{FIR} provides the total FIR flux for $\lambda > 50 \mu\text{m}$. Noting that $f_{\nu}(90 \mu\text{m}) = \Omega \tau_{90} B_{\nu}(90 \mu\text{m}, T_d)$, we obtain the following expression similar to that of Nagata et al. (2002):

$$f_{FIR} \simeq C_1 f_{\nu}(65 \mu\text{m}) + f_{\nu}(90 \mu\text{m}) \left[\exp \left(\frac{159.8}{T_d} \right) - 1 \right] \times \left[C_2 T_d^{\beta+4} - \frac{C_3}{\exp(221.3/T_d) - 1} \right], \quad (6)$$

where $C_1 = 1.58 \times 10^{12} \text{ Hz}$, $C_2 = 795.6 \text{ Hz K}^{-5}$ and 24.42 Hz K^{-6} for $\beta = 1$ and 2, respectively, and $C_3 = 8.262 \times 10^{12} \text{ Hz}$ and $1.144 \times 10^{13} \text{ Hz}$ for $\beta = 1$ and 2, respectively.

By using f_{FIR} , we obtain the total FIR luminosity L_{FIR} as

$$L_{FIR} = 4\pi D^2 f_{FIR}, \quad (7)$$

where D is the distance to the object. In Table 4, we present the estimated FIR luminosities for the sample. The FIR luminosities estimated with $\beta = 1$ and 2 are indicated by $L_{FIR}(\beta = 1)$ and $L_{FIR}(\beta = 2)$, respectively. For Mrk 36, it is not possible to determine L_{FIR} since T_d cannot be determined. Thus, we exclude Mrk 36 from the analysis here. The error of L_{FIR} mainly comes from the uncertainty in the flux estimation ($\sim 20\%$). We note that the uncertainty caused by the difference in β is comparable to or smaller than 20%.

Table 5. Correction factor (C_{AKARI}) multiplied to the AKARI FIR luminosity to obtain the total FIR luminosity.

β	Spiral sample	
	included	not included
1	1.36 ± 0.17	1.34 ± 0.19
2	1.19 ± 0.10	1.22 ± 0.11

Note. The number after “ \pm ” shows the standard deviation (1σ).

It is convenient to obtain a conversion formula from the AKARI FIR luminosity to the total FIR luminosity. We define the “correction” factor, C_{AKARI} , which is to be multiplied to the AKARI FIR luminosity to obtain the total FIR luminosity as

$$L_{FIR}(\beta) = C_{AKARI}(\beta) L_{AKARI}, \quad (8)$$

where L_{FIR} and thus C_{AKARI} depend on the assumed value of β . Because the sample size is small, we cannot investigate the possible dependence of C_{AKARI} on various physical parameters such as dust temperature. Thus, we only estimate the average of C_{AKARI} for the sample. The results are listed in Table 5, where the averages of C_{AKARI} with and without the spiral sample are shown. We see that there is no significant difference in C_{AKARI} between those two averages. On the other hand, there seems to be difference in C_{AKARI} between $\beta = 1$ and 2, mainly because the extrapolation to long wavelengths ($\lambda > 170 \mu\text{m}$) in estimating the total FIR luminosity depends on β . In summary, we can convert the AKARI FIR luminosity to the total FIR luminosity by multiplying 1.2–1.4. We note that a further 30–40% correction for the contribution from mid-infrared emission at $\lambda < 50 \mu\text{m}$ will be necessary to estimate the total infrared luminosity of dust emission (Dale & Helou 2002).

4.4. Star formation rate

It is empirically known that the FIR luminosity is a good indicator of the SFR. Hirashita, Buat, & Inoue (2003) provide a conversion formula from L_{FIR} to SFR (we assume that L_{IR} in Hirashita, Buat, & Inoue 2003 is approximated by L_{FIR} , but as mentioned in section 4.3, the upward 30–40% correction for $\lambda < 50 \mu\text{m}$ may be required for L_{FIR}):

$$\text{SFR} = C_{\text{IR}} L_{\text{FIR}}, \quad (9)$$

where we adopt the conversion coefficient $C_{\text{IR}} = 2.0 \times 10^{-10} M_{\odot} \text{yr}^{-1} L_{\odot}^{-1}$ as recommended by Hirashita, Buat, & Inoue (2003). The SFR estimated by using $L_{\text{FIR}}(\beta = 1)$ is listed in Table 6 for each galaxy. If we adopt $L_{\text{FIR}}(\beta = 2)$, we obtain smaller SFR by 4–26%. The range of the SFR is 0.01–0.4 $M_{\odot} \text{yr}^{-1}$ for the present BCD sample. This is within the range (a few times 10^{-3} to several times $10 M_{\odot} \text{yr}^{-1}$) given for a BCD sample by Hopkins, Schulte-Ladbeck, & Drozdovsky (2002).

There are two common BCDs between this paper and Hopkins, Schulte-Ladbeck, & Drozdovsky (2002): Mrk 71 and Mrk 36. For the latter galaxy, we do not obtain the SFR because it is not possible to determine L_{FIR} (section 4.3). For Mrk 71, our estimate is 2–3 times lower than their estimate ($0.065 M_{\odot} \text{yr}^{-1}$ from the IRAS 60 μm luminosity and $0.041 M_{\odot} \text{yr}^{-1}$ from the 1.4 GHz radio luminosity). This confirms the comment of Hirashita, Buat, & Inoue (2003) that there is a risk of underestimating the SFR for $\text{SFR} \lesssim 1 M_{\odot} \text{yr}^{-1}$ if we use equation (9). This may be because of smaller dust optical depth.

There are three overlapping BCDs between this paper and Sage et al. (1992): II Zw 40, UM 439, and UM 533. Their SFR derived from the FIR luminosity (0.46, 0.085, and $0.049 M_{\odot} \text{yr}^{-1}$, respectively) is systematically higher, which is attributed to different C_{IR} ($6.5 \times 10^{-9} M_{\odot} \text{yr}^{-1} L_{\odot}^{-1}$). This high C_{IR} is consistent with the SFR derived from $\text{H}\alpha$ luminosity in dwarf galaxies (Thronson & Telesco 1986), which again confirms the necessity of using higher C_{IR} than proposed by Hirashita, Buat, & Inoue (2003) for $\text{SFR} \lesssim 1 M_{\odot} \text{yr}^{-1}$. Moreover, the SFR derived from $\text{H}\alpha$ in Sage et al. (1992) (3.1, 0.20, and $0.19 M_{\odot} \text{yr}^{-1}$, respectively) is much higher than SFR derived from the FIR luminosity, which is again explained by small dust optical depth as mentioned in the previous paragraph. However, the SFR derived from $\text{H}\alpha$ luminosity in Sage et al. (1992) could be overestimated because they assume that 2/3 of the ionizing photons are absorbed by dust, which might be less in low-metallicity galaxies like BCDs.

4.5. Dust mass

As stated in section 1, the *WIDE-S* (90 μm) and *WIDE-L* (140 μm) bands are suitable to trace the total mass of large grains which have the dominant contribution to the total dust content. The total dust mass M_{d} is related to the flux as (e.g., Hildebrand 1983)

$$M_{\text{d}} = \frac{F_{\nu}(\lambda) D^2}{\kappa_{\nu} B_{\nu}(T_{\text{d}})}, \quad (10)$$

where κ_{ν} is the mass absorption coefficient of dust grains. For simplicity, we assume spherical grains with a single radius a and with a uniform density s . As shown later, the assumption on a is not essential, since κ_{ν} is insensitive to a . The cross section of a grain is expressed as $\pi a^2 Q_{\nu}$, where Q_{ν} is a dimensionless quantity expressing the emission efficiency. Using Q_{ν} , the mass absorption coefficient is written as

$$\kappa_{\nu} = \frac{3Q_{\nu}}{4as}. \quad (11)$$

Since there is a relation of $Q_{\nu} \propto a$ for $a \ll \lambda$ (Evans 1995), the estimate of κ_{ν} is insensitive to the assumed value of a . Hildebrand (1983) estimates Q_{ν}/a at $\lambda = 125 \mu\text{m}$ to be $3/400 \mu\text{m}^{-1}$. We note that the normalization of Q_{ν}/a at $\lambda = 125 \mu\text{m}$ is convenient since it is roughly the middle of the two wavelengths ($\lambda = 90 \mu\text{m}$ and $140 \mu\text{m}$) used for the estimate of dust mass. If we adopt $s = 3 \text{ g cm}^{-3}$, we obtain

$$\kappa_{\nu} = 18.8 \left(\frac{\lambda}{125 \mu\text{m}} \right)^{-\beta} \text{ cm}^2 \text{ g}^{-1}. \quad (12)$$

In Table 4, we list the dust mass, where we adopt $T_{\text{d}}([140/90])$ for the dust temperature. The dust mass estimated with $\beta = 1$ and 2 are denoted as $M_{\text{d}}(\beta = 1)$ and $M_{\text{d}}(\beta = 2)$, respectively. The dust mass in Mrk 36 is given by using the $T_{\text{d}}([65/90])$ instead of $T_{\text{d}}([140/90])$, for which only a lower limit is given. Since $T_{\text{d}}([65/90])$ tends to overestimate the equilibrium grain temperature (section 4.1), we regard this dust mass to be a lower limit. From Table 4, we observe that $M_{\text{d}}(\beta = 1)$ is systematically lower than $M_{\text{d}}(\beta = 2)$ by a factor of 2.5. This is because higher dust temperature for $\beta = 1$ leads to a lower dust mass with a fixed dust emissivity.

One of our BCDs, II Zw 40, overlaps with the sample in Galliano et al. (2005) (section 3.3), who model the dust SED. First of all, the mass of the big grain component, which is contributing to the FIR regime, is just the same as our estimate ($1.1 \times 10^5 M_{\odot}$) if we adopt $\beta = 2$. This means that the AKARI *WIDE-S* (90 μm) and *WIDE-L* (140 μm) bands are indeed useful to trace the dust mass. However, they also show an additional very cold dust component contributing to the emission at submillimeter wavelengths, although the amount of this component is dependent on the FIR emissivity index β . This very cold component cannot be investigated by AKARI, and we concentrate on the dust component contributing to the FIR emission in this paper.

5. Discussion

5.1. Star formation properties

In section 4.2, we have shown that the BCD sample tends to show higher UV radiation fields than spiral galaxies. This is consistent with a picture that intense star formation is occurring in a concentrated region in BCDs. In order to examine the properties of such an intense star formation activity (e.g., a burst or a continuous mode of star formation) it is useful to estimate the gas consump-

Table 6. Some related quantities used for discussion.

Name	SFR* [$M_{\odot} \text{ yr}^{-1}$]	M_{HI} [M_{\odot}]	τ_{SF} [Gyr]	$12 + \log(\text{O}/\text{H})$	\mathcal{D}
II Zw 40	0.22	2.0×10^8	0.91	8.15	2.0×10^{-4}
Mrk 7	0.50	3.6×10^9	7.2	8.54	3.9×10^{-4}
Mrk 71	0.012	1.2×10^9	110	7.83	4.5×10^{-6}
UM 439	0.021	1.7×10^8	8.1	7.98	8.2×10^{-5}
UM 533	0.020	5.8×10^7	2.9	8.10	3.8×10^{-4}
II Zw 70	0.073	3.6×10^8	4.9	8.11	2.3×10^{-4}
II Zw 71	0.080	7.3×10^8	9.1	8.24	1.4×10^{-3}
Mrk 36	— [†]	1.8×10^7	< 2.5	7.81	$> 4.6 \times 10^{-5}$

Note. Lower and upper limits are shown by “>” and “<”, respectively. For Mrk 36, SFR cannot be estimated.

* The SFR is derived by using $L_{\text{FIR}}(\beta = 1)$. If $L_{\text{FIR}}(\beta = 2)$ is used instead, the SFR becomes 4–26% higher according to the difference in L_{FIR} .

[†] The SFR of Mrk 36 cannot be estimated because L_{FIR} is not available.

tion timescale (τ_{SF}) as follows.

Here, we adopt the SFR estimated in section 4.4 by adopting $L_{\text{FIR}}(\beta = 1)$. (If we adopt $L_{\text{FIR}}(\beta = 2)$, the gas consumption timescale becomes 4–26% shorter.) Then the gas consumption timescale is defined as the gas mass divided by the SFR. For the gas mass, we adopt the mass of HI gas (M_{HI}) in the same way as in Hirashita, Tajiri, & Kamaya (2002) and Hopkins, Schulte-Ladbeck, & Drozdovsky (2002), since molecular gas is rarely detected for BCDs (Barone et al. 2000). We estimate M_{HI} of II Zw 71 by using the HI flux measured by Huchtmeier & Richter (1989) and by using equation (1) in Lisenfeld & Ferrara (1998). The estimated gas consumption time τ_{SF} is listed in Table 6. We observe that τ_{SF} is distributed with a range of two orders of magnitude, which is consistent with Hopkins, Schulte-Ladbeck, & Drozdovsky (2002). Moreover, the gas consumption time does not correlate with G_{UV} . For example, Mrk 71 has large G_{UV} , which indicates a concentrated intense star formation, but has large τ_{SF} exceeding the cosmic timescale. Such galaxies with long τ_{SF} but high G_{UV} give us a picture that the star formation is strongly activated only in a limited region. On the contrary, II Zw 40 has large G_{UV} and small τ_{SF} , indicating the whole galaxy may be in an active phase of star formation.

It is possible that the star formation in BCDs is intermittent. In this case, the diversity in τ_{SF} is naturally explained: if a BCD is in activated/inactivated phase of star formation, τ_{SF} becomes small/large. Indeed, the effect of feedback is considered to be enhanced in small systems such as BCDs, leading to an intermittent nature of star formation (Saitō, Kamaya, & Tomita 2000; Carraro et al. 2001; Kobayashi & Kamaya 2004; Kamaya 2005). It is also observationally suggested that the star formation in dwarf galaxies may be episodic (Fanelli, O’Connell, & Thuan 1988; Greggio et al. 1998; Grossi et al. 2007).

5.2. Dust-to-gas ratio and chemical enrichment

The dust production is strongly related to the metal production. Indeed, the relation between dust abundance (usually dust-to-gas ratio is adopted) and metal abun-

dance (metallicity) can be investigated by using chemical evolution models (Dwek 1998; Hirashita, Tajiri, & Kamaya 2002). Here we consider whether dust-to-gas ratio and metallicity are related or not.

As the metal abundance, we adopt oxygen abundance, which is the most easily observed. The oxygen abundance of each sample BCD is compiled in Hirashita, Tajiri, & Kamaya (2002) and Hopkins, Schulte-Ladbeck, & Drozdovsky (2002), but for II Zw 71 we take the oxygen abundance from Kewley, Jansen, & Geller (2005). The dust-to-gas ratio \mathcal{D} is estimated by $M_{\text{d}}(\beta = 1)$ divided by M_{HI} . If we use $M_{\text{d}}(\beta = 2)$ instead, we obtain about 2.5 times higher dust-to-gas ratio. Note that the dust-to-gas ratio would shift further upward if there is really a very cold dust component contributing to longer wavelengths than those traced by AKARI (Galliano et al. 2005; section 4.5). In Table 6, we list the metallicity (oxygen abundance: $12 + \log(\text{O}/\text{H})$) and the dust-to-gas ratio \mathcal{D} . Note that the solar abundance is $12 + \log(\text{O}/\text{H}) = 8.93$ (Anders & Grevesse 1989).

In Figure 2, we show the relation between those two quantities. We observe that there is a positive correlation between dust-to-gas ratio and metallicity. This correlation is also shown by Engelbracht et al. (2008) with a larger metallicity range. The correlation is consistent with the picture that dust enrichment proceeds as the system is enriched by metals.

It is also interesting to compare the results with theoretical model predictions. Here we adopt a model by Hirashita, Tajiri, & Kamaya (2002) (originally developed by Lisenfeld & Ferrara 1998), who consider a one-zone chemical evolution model with the instantaneous recycling approximation (Tinsley 1980). The model equations consist of the evolutions of gas mass, metal mass, and dust mass. By treating these equations, the relation between dust-to-gas ratio and metallicity is obtained. In particular, there are two important parameters in the model: (i) the fraction of metals condensed into dust grains, f_{in} , and (ii) the “dust destruction efficiency”, β_{SN} . The former parameter is fixed to 0.1, and does not contribute to the scatter of the dust-to-gas ratio if the condensa-

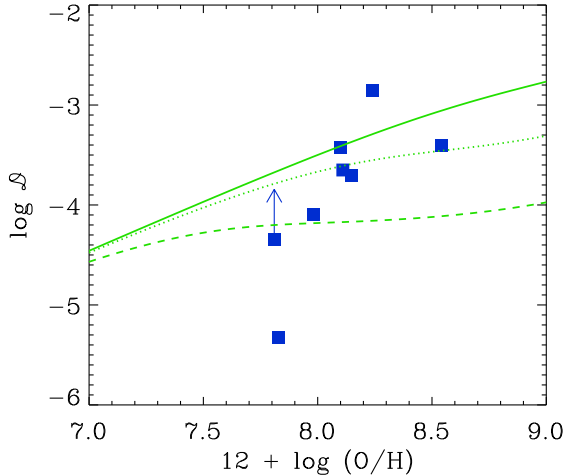


Fig. 2. Relation between dust-to-gas ratio \mathcal{D} and metallicity. The data of the present BCD sample are shown by solid squares. The arrow indicates a lower limit. The solid, dotted, and dashed lines show the model predictions by Hirashita, Tajiri, & Kamaya (2002) with various dust destruction efficiencies (in their notation $\beta_{\text{SN}} = 1, 5,$ and 25 , respectively).

tion efficiency in the stellar mass loss is independent of age. The “dust destruction efficiency” β_{SN} is defined as $\beta_{\text{SN}} \equiv M_{\text{g}}/(\tau_{\text{SN}}\psi)$, where M_{g} is the total gas mass, τ_{SN} is the timescale of dust destruction by supernova shocks, and ψ is the SFR. This parameter can be expressed as follows (Hirashita, Tajiri, & Kamaya 2002, equation 6):

$$\beta_{\text{SN}} = \epsilon M_{\text{s}} \frac{\gamma}{\psi} \frac{1}{X_{\text{SF}}}, \quad (13)$$

where ϵ is the fraction of destroyed dust in a SN blast, M_{s} is the gas mass accelerated to a velocity large enough for dust destruction (typically 100 km s^{-1}), γ is the supernova rate, and X_{SF} is the gas mass fraction in the star-forming region, where the dust formation and destruction are really occurring (the rest of the gas is considered to be contained in the H I envelope, which they assume not to be concerned with the dust formation and destruction). Typical values are $\epsilon \sim 0.1$ (McKee 1989), $M_{\text{s}} \sim 6800 M_{\odot}$ (if we adopt 10^{51} erg for the kinetic energy input of a supernova, and 100 km s^{-1} for the threshold velocity for the dust destruction), $\gamma/\psi \sim 1/136 M_{\odot}$ (for the Galaxy; Lisenfeld & Ferrara 1998), we obtain $\beta_{\text{SN}} = 5$ for $X_{\text{SF}} = 1$. Hirashita, Tajiri, & Kamaya (2002) argue that this parameter changes according to the relative contribution between Type Ia supernovae and Type II supernovae. If an intermittent star formation activity is assumed, γ/ψ can change by a factor of 20 (Bradamante, Matteucci, & D’Ercole 1998; Hirashita, Tajiri, & Kamaya 2002). Motivated by this factor, they changed β_{SN} from 1 to 25.

In Figure 2, we show the theoretical predictions for $\beta = 1, 5,$ and 25 with $f_{\text{in}} = 0.1$. We observe that those models explain the data points except for the two extremes (II Zw 71 and Mrk 71 for the upper and lower

extremes in Figure 2, respectively). The variation in β_{SN} increases the scatter of the dust-to-gas ratio at a certain metallicity and makes the correlation less clear. Further change of β_{SN} may be possible because of the change of X_{SF} . As mentioned in section 5.1, only a small fraction of gas may be concerned with star formation in Mrk 71. Thus, $X_{\text{SF}} \ll 1$ is expected for Mrk 71, where β_{SN} could be larger than the above values. Such a large value of β_{SN} may explain the extremely poor dust-to-gas ratio of Mrk 71.

As commented above, the dust-to-gas ratios are larger if we adopt $\beta = 2$, and/or if the cold dust component contributing to the submillimeter wavelengths, which we fail to trace in FIR, really exists as proposed by Galliano et al. (2005). In these cases, we should adopt a larger f_{in} , but a large variation of β_{SN} is still required to explain the large scatter of dust-to-gas ratios.

6. Summary

We have reported far-infrared (FIR) properties of eight blue compact dwarf galaxies (BCDs) observed by AKARI. The fluxes at wavelengths of $65 \mu\text{m}$, $90 \mu\text{m}$, $140 \mu\text{m}$, and $160 \mu\text{m}$ are measured and are used to estimate basic quantities about dust grains such as dust temperature, dust mass, and total FIR luminosity. We have found that the typical dust temperature of our BCD sample, except for Mrk 7 and II Zw 71, is significantly higher than that of normal spiral galaxies. This indicates high interstellar radiation field, which proves to range up to 100 times the Galactic value. This confirms the concentrated star-forming activity in BCDs. The star formation rate (SFR) is also evaluated from the FIR luminosity as $0.01\text{--}0.5 M_{\odot} \text{ yr}^{-1}$. Combining this quantity with gas mass taken from the literature, we estimate the gas consumption timescales (gas mass divided by SFR), which span a wide range from 1 Gyr to 100 Gyr. A natural interpretation of this large variety can be provided by intermittent star formation activity. We finally show the relation between dust-to-gas ratio and metallicity (we utilize our estimate of dust mass, and take other necessary quantities from the literature). There is a positive correlation between dust-to-gas ratio and metallicity as expected from chemical evolution models.

We are grateful to S. Madden, the referee, for her helpful comments that improved this paper very much. We thank H. Shibai, Y. Y. Tajiri, M. Nagaoka, Y. Doi, S. Matsuura, and M. Shirahata for useful discussions about observations and data analysis. We thank all members of AKARI project for their continuous help and support. This research has made use of the NASA/IPAC Extragalactic Database (NED), which is operated by the Jet Propulsion Laboratory, California Institute of Technology, under contract with the National Aeronautics and Space Administration.

References

- Anders, E., & Grevesse, N. 1989, *Geochim. Cosmochim. Acta*, 53, 197
- Barone, L. T., Heithausen, A., Hüttemeister, Fritz, T., & Klein, U. 2000, *MNRAS*, 317, 649
- Beck, S. C., Turner, J. L., Langland-Shula, L. E., Meier, D. S., Crosthwaite, L. P., & Gorjian, V. 2002, *AJ*, 124, 2516
- Bertoldi, F., Carilli, C. L., Cox, P., Fan, X., Strauss, M. A., Beelen, A., Omont, A., Zylka, R. 2003, *A&A*, 406, L55
- Bianchi, S., & Schneider, R. 2007, *MNRAS*, 378, 973
- Bradamante, F., Matteucci, F., & D'Ercole, A. 1998, *A&A*, 337, 338
- Buat, V., & Xu, C. 1996, *A&A*, 306, 61
- Carraro, G., Chiosi, C., Girardi, L., & Lia, C. 2001, *MNRAS*, 327, 69
- Ciardi, B., Bianchi, S., & Ferrara, A. 2002, *MNRAS*, 331, 463
- Dale, D. A., & Helou, G. 2002, *ApJ*, 576, 159
- Draine, B. T., & Anderson, N. 1985, *ApJ*, 292, 494
- Draine, B. T., & Li, A. 2001, *ApJ*, 551, 807
- Dunne, L., Eales, S., Ivison, R., Morgan, H., & Edmunds, M. 2003, *Nature*, 424, 285
- Dwek, E. 1998, *ApJ*, 501, 643
- Dwek, E., Galliano, F., Jones, A. P. 2007, *ApJ*, 662, 927
- Dwek, E., & Scalo, J. M. 1980, *ApJ*, 239, 193
- Engelbracht, C. W., Rieke, G. H., Gordon, K. D., Smith, J.-D. T., Werner, M. W., Moustakas, J., Willmer, C. N. A., & Vanzi, L. 2008, *ApJ*, 678, 804
- Ercolano, B., Barlow, M. J., & Sugerman, B. E. K. 2007, *MNRAS*, 375, 753
- Evans, A. 1995, *The Dusty Universe* (New York: Wiley)
- Fanelli, M. N., O'Connell, R. W., & Thuan, T. X. 1988, *ApJ*, 334, 665
- Galliano, F., Madden, S. C., Jones, A. P., Wilson, C. D., & Bernard, J.-P. 2005, *A&A*, 434, 867
- Greggio, L., Tosi, M., Clampin, M., De Marchi, G., Leitherer, C., Nota, A., & Sirianni, M. 1998, *ApJ*, 504, 725
- Grossi, M., Disney, M. J., Pritzl, B. J., Knezek, P. M., Gallagher, J. S., Minchin, R. F., & Freeman, K. C. 2007, *MNRAS*, 374, 107
- Hibi, Y., Shibai, H., Kawada, M., Ootsubo, T., & Hirashita, H. 2006, *PASJ*, 58, 509
- Hildebrand, R. H. 1983, *QJRAS*, 24, 267
- Hines, D. C., et al. 2004, *ApJS*, 154, 290
- Hirashita, H., Buat, V., & Inoue, A. K. 2003, *A&A*, 410, 83
- Hirashita, H., & Ferrara, A. 2002, *MNRAS*, 337, 921
- Hirashita, H., Hibi, Y., & Shibai, H. 2007, *MNRAS*, 379, 974
- Hirashita, H., Nozawa, T., Takeuchi, T. T., & Kozasa, T. 2008, *MNRAS*, 384, 1725
- Hirashita, H., Tajiri, Y. Y., & Kamaya, H. 2002, *A&A*, 388, 439
- Hoffman, G. L., Helou, G., Salpeter, E. E., & Lewis, B. M. 1989, *ApJ*, 339, 812
- Hopkins, A. M., Schulte-Ladbeck, R. E., & Drozdovsky, I. O. 2002, *AJ*, 124, 862
- Huchtmeier, W. K., & Richter, O.-G. 1989, *A General Catalog of H I Observations of Galaxies* (New York: Springer)
- Hunt, L. K., Bianchi, S., & Maiolino, R. 2005, *A&A*, 434, 849
- Hunt, L. K., Thuan, T. X., Sauvage, M., & Izotov, Y. I. 2006, *ApJ*, 653, 222
- Inoue, A. K., Hirashita, H., & Kamaya, H. 2000, *PASJ*, 52, 539
- Jeong, W.-S., et al. 2007, *PASJ*, 59, S429
- Jurcevic, J. S., & Butcher, D. 2006, *Bulletin of the American Astronomical Society*, 38, 92
- Kamaya, H. 2005, *A&A*, 434, 163
- Kaneda, H., et al. 2007, *PASJ*, 59, S463
- Karachentsev, I. D., et al. 2002, *A&A*, 383, 125
- Kawada, M., et al. 2007, *PASJ*, 59, S389
- Kennicutt, R. C., Jr. 1998, *ARA&A*, 36, 189
- Kewley, L. J., Jansen, R. A., & Geller, M. J. 2005, *PASP*, 117, 227
- Kobayashi, M. A. R., & Kamaya, H. 2004, *A&A*, 425, L41
- Kozasa, T., Hasegawa, H., & Nomoto, K. 1989, *ApJ*, 344, 325
- Le Floc'h, E., et al. 2005, *ApJ*, 632, 169
- Li, A., & Draine, B. T. 2001, *ApJ*, 554, 778
- Lisenfeld, U., & Ferrara, A. 1998, *ApJ*, 496, 145
- Maiolino, R., Schneider, R., Oliva, E., Bianchi, S., Ferrara, A., Mannucci, F., Pedani, M., & Roca Sogorb, M. 2004, *Nature*, 431, 533
- Mathis, J. S., Rumpl, W., & Nordsieck, K. H. 1977, *ApJ*, 217, 425
- Mazzarella, J. M., Bothun, G. D., & Boroson, T. A. 1991, *AJ*, 101, 2034
- McKee, C. F. 1989, in *Interstellar Dust*, ed. L. J. Allamandola, & A. G. G. M. Tielens (Dordrecht: Kluwer), IAU Symp. 135, 431
- Meikle, W. P. S., et al. 2007, *ApJ*, 665, 608
- Morgan, H. L., & Edmunds, M. G. 2002, *MNRAS*, 343, 427
- Moseley, S. H., Dwek, E., Glaccum, W., Graham, J. R., & Loewenstein, R. F. 1989, *Nature*, 340, 697
- Moshir, M., et al. 1990, *IRAS Faint Source Catalog, Version 2.0* (Pasadena: Infrared Processing and Analysis Center)
- Murakami, H., et al. 2007, *PASJ*, 59, S369
- Nagata, H., Shibai, H., Takeuchi, T. T., & Onaka, T. 2002, *PASJ*, 54, 695
- Neugebauer, G., et al. 1984, *ApJ*, 278, L1
- Noeske, K. G., Guseva, N. G., Fricke, K. J., Izotov, Y. I., Papaderos, P., & Thuan, T. X. 2000, *A&A*, 361, 33
- Nozawa, T., Kozasa, T., Umeda, H., Maeda, K., & Nomoto, K. 2003, *ApJ*, 598, 785
- Okumura, K., Hiromoto, N., Shibai, H., Onaka, T., Nakagawa, T., Matsuhara, H., Makiuti, S., & Okuda, H. 2002, *Adv. Space Res.*, 30, 2037
- Osman, A. M. I., Ella, M. S., & Issa, I. A. 1982, *Astron. Nachr.* 303, 329
- Pérez-González, P. G., et al. 2005, *ApJ*, 630, 82
- Plante, S., & Sauvage, M. 2002, *AJ*, 124, 1995
- Popescu, C. C., Tuffs, R. J., Völk, H. J., Pierini, D., & Madore, B. F. 2002, *ApJ*, 567, 221
- Priddey, R. S., Isaak, K. G., McMahan, R. G., Robson, E. I., & Pearson, C. P. 2003, *MNRAS*, 344, L74
- Rho, J., et al. 2008, *ApJ*, 673, 271
- Sage, L. J., Salzer, J. J., Loose, H.-H., & Henkel, C. 1992, *A&A*, 265, 19
- Saitō, M., Kamaya, H., & Tomita, A. 2000, *PASJ*, 52, 821
- Sargent, W. L. W., & Searle, L. 1970, *ApJ*, 162, L155
- Shibai, H., Okumura, K., & Onaka, T. 1999, in *Star Formation 1999*, ed. T. Nakamoto (Nobeyama: Nobeyama Radio Observatory), 67
- Steidel, C. C., Adelberger, K. L., Giavalisco, M., Dickinson, K., Pettini, M. 1999, *ApJ*, 519, 1
- Sugerman, B. E. K., et al. 2006, *Science*, 313, 196
- Suzuki, T., et al. 2008, *PASJ*, in this volume
- Suzuki, T., Kaneda, H., Nakagawa, T., Makiuti, S., & Okada, Y. 2007, *PASJ*, 59, S473

- Takeuchi, T. T., Buat, V., & Burgarella, D. 2005, *A&A*, 440, L17
- Takeuchi, T. T., Ishii, T. T., Nozawa, T., Kozasa, T., & Hirashita, H. 2005, *MNRAS*, 362, 592
- Thronson, H. A., Jr., & Telesco, C. M. 1986, *ApJ*, 311, 98
- Thuan, T. X., Sauvage, M., & Madden, S. 1999, *ApJ*, 516, 783
- Tinsley, B. M. 1980, *Fundam. Cosmic Phys.*, 5, 287
- Tolstoy, E., Saha, A., Hoessel, J. G. McQuade, K. 1995, *AJ*, 110, 1640
- Vader, J. P., Frogel, J. A., Terndrup, D. M., & Heisler, C. A. 1993, *AJ*, 106, 1743
- Vanzi, L., Cresci, G., Teles, E., & Melnick, J. 2008, *A&A*, 486, 393
- Verdugo, E., Yamamura, I., & Pearson, C. P. 2007, *AKARI FIS Data User Manual Version 1.2*